nature physics

ARTICLES

https://doi.org/10.1038/s41567-022-01747-0

Check for updates

Collective curvature sensing and fluidity in three-dimensional multicellular systems

Wenhui Tang[1], Amit Das[2], Adrian F. Pegoraro[3,8], Yu Long Han[1], Jessie Huang[4,5], David A. Roberts[4], Haiqian Yang[1], Jeffrey J. Fredberg[6], Darrell N. Kotton[4,5,7], Dapeng Bi[2] and Ming Guo[1]✉

Collective cell migration is an essential process throughout the lives of multicellular organisms, for example in embryonic development, wound healing and tumour metastasis. Substrates or interfaces associated with these processes are typically curved, with radii of curvature comparable to many cell lengths. Using both artificial geometries and lung alveolospheres derived from human induced pluripotent stem cells, here we show that cells sense multicellular-scale curvature and that it plays a role in regulating collective cell migration. As the curvature of a monolayer increases, cells reduce their collectivity and the multicellular flow field becomes more dynamic. Furthermore, hexagonally shaped cells tend to aggregate in solid-like clusters surrounded by non-hexagonal cells that act as a background fluid. We propose that cells naturally form hexagonally organized clusters to minimize free energy, and the size of these clusters is limited by a bending energy penalty. We observe that cluster size grows linearly as sphere radius increases, which further stabilizes the multicellular flow field and increases cell collectivity. As a result, increasing curvature tends to promote the fluidity in multicellular monolayer. Together, these findings highlight the potential for a fundamental role of curvature in regulating both spatial and temporal characteristics of three-dimensional multicellular systems.

Collective cellular migration has been widely observed in embryonic development[1–3], wound healing[4,5] and tumour invasion[6,7]. From the perspectives of both biophysics and signalling, collective cellular migration[8–11] and the associated issues of packing geometry[12–15] and cell jamming and unjamming[16–21] on two-dimensional (2D) flat surfaces have been widely explored. For example, epithelial cells growing on flat substrates approach a jamming transition during maturation, exhibiting an increasing velocity correlation length[9], decreasing cell speed[9,22] and decreasing cell aspect ratio[23]. In contrast, most biological structures, such as alveoli, bronchi and intestines, are naturally curved in three dimensions. Even for inert materials, it is known that curvature fundamentally changes basic processes such as crystallization[24,25], yet it remains unclear to what extent the cellular collective responds to curvature.

At the subcellular scale, previous studies have shown that certain proteins, such as clathrin and dynamin 2 on cell membranes, can sense curvatures with radii <200 nm (ref. [26]). Yet many biological systems have radii of curvature that vary from tens to hundreds of micrometres, corresponding to cellular and multicellular levels. Interestingly, curvatures in this range have recently been shown to affect a variety of cell behaviours[27–30]. In particular, when cell monolayers are cultured on a tubular surface, tube diameters on the order of several cell lengths have been shown to promote cell alignment and migration longitudinally along the tube axis[27,28]. Cells cultured on wavy structures with curvature radius of less than five cell lengths exhibit an obvious change of cell height depending on the sign of substrate curvature[29,30]. These results highlight the influence of curvature on cell behaviour, but do not determine whether cells are sensitive to inherent curvature or differential curvature. All surfaces are defined locally by two principal radii of curvature. In tubular and wavy geometries, these radii are discordant, and cells necessarily exist in an anisotropic environment. Take tubular geometries as an example: as the radius of curvature in the axial direction is fixed, curvature changes in the other dimension, and both the inherent and differential curvature change in concert. Using geometries with uniform curvature in all directions—spherical geometries—would allow the effect of curvature on cellular migration to be directly measured.

Here we investigate the role of curvature in regulating collective cellular behaviour on spherical three-dimensional (3D) surfaces using a combination of experiments and in silico modelling. Our results reveal that the migratory speed of the individual cell is largely unaffected by curvature, whereas the collective migration of the cells becomes more dynamic, less coherent and more heterogeneous. Conversely, as curvature decreases cells become hexagonally coordinated into progressively larger spatial packs. On the basis of results from simulations and in vitro experiments, we propose that this behaviour is a direct consequence of hexagonal cells being more solid-like whereas non-hexagonal cells are more fluid-like. Moreover, due to their solidity, the hexagonal clusters on a curved surface incur an elastic bending energy. Together, the interplay of the energetic cost of bending and the energetic preference towards solidification gives rise to the observed organization of cellular packs, leading to a series of curvature-dependent collective cellular behaviours.

To mimic the typical size of curved biological structures in situ, we fabricated hemispherical structures with both positive and negative radii of curvature (125, 225 and 325 μm; Fig. 1a,b) using

[1]Department of Mechanical Engineering, Massachusetts Institute of Technology, Cambridge, MA, USA. [2]Department of Physics, Northeastern University, Boston, MA, USA. [3]Department of Physics, University of Ottawa, Ottawa, Ontario, Canada. [4]Center for Regenerative Medicine of Boston University and Boston Medical Center, Boston, MA, USA. [5]The Pulmonary Center and Department of Medicine, Boston University School of Medicine, Boston, MA, USA. [6]Harvard T. H. Chan School of Public Health, Boston, MA, USA. [7]Department of Pathology & Laboratory Medicine, Boston University School of Medicine, Boston Medical Center, Boston, MA, USA. [8]Present address: Metrology Research Centre, National Research Council Canada, Ottawa, Ontario, Canada. ✉e-mail: guom@mit.edu

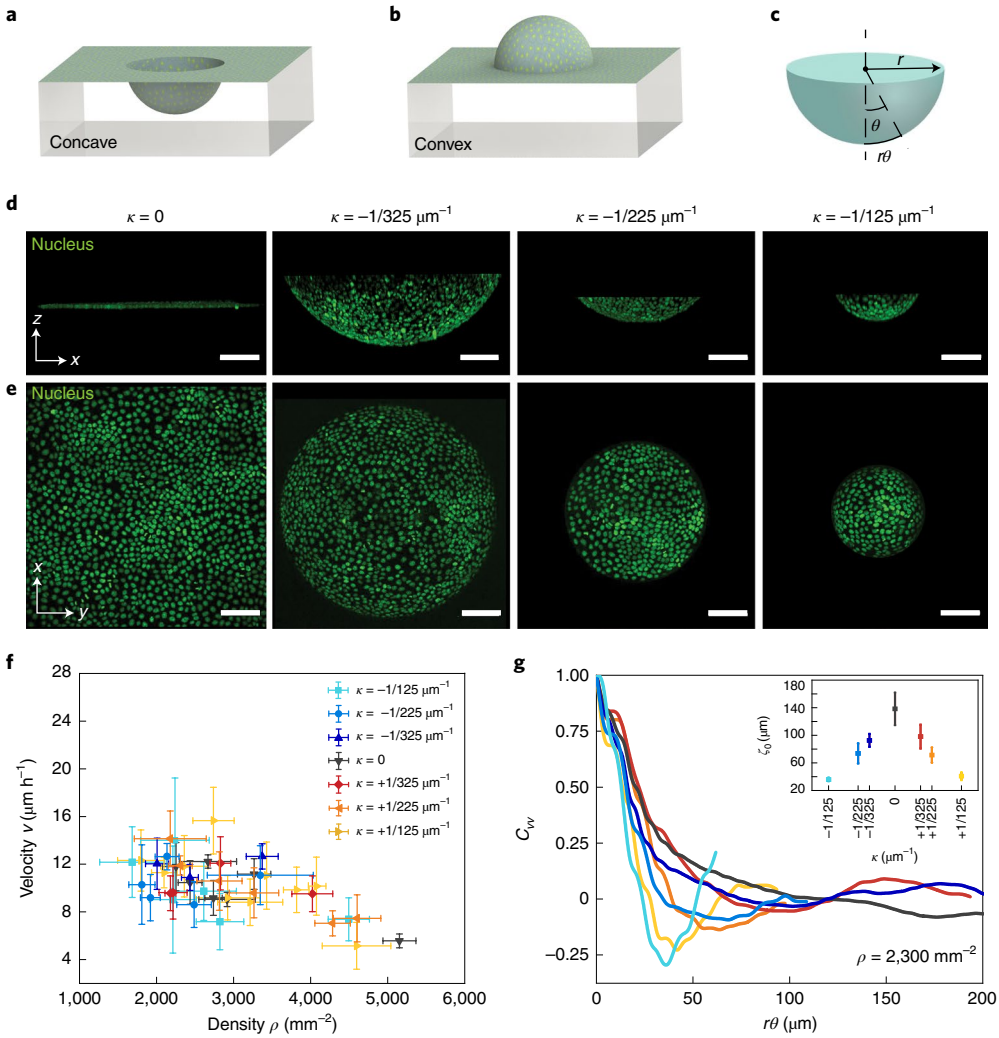

Fig. 1 | MDCK cells grown on different curvatures and their individual and collective cellular behaviours. a,**b**, Schematics of cells grown on 3D PDMS hemispheres with negative/concave (**a**) and positive/convex curvatures (**b**). **c**, Schematic showing the sphere, r, θ and $r\theta$. **d**, Side view of 3D reconstructed images (using Leica LAS X) of MDCK cells grown on flat surfaces and wells with 650 μm, 450 μm and 250 μm diameters (left to right) (curvatures κ of 0, −1/325 μm^{-1}, −1/255 μm^{-1} and −1/125 μm^{-1}). Scale bars, 100 μm. **e**, Top view (maximum intensity projection) of NLS-GFP-labelled MDCK nuclei on PDMS hemispheres. Scale bars, 100 μm. **f**, Average cell speed as a function of cell density for different κ. Each point is an average of 10–20 consecutive frames (15 min per frame) from the same well. Error bars show 1 s.d. Each frame contains several hundred cells. **g**, Representative group C_{vv} and ζ_0 (inset) values for cells with $\rho = 2{,}300$ mm^{-2} for different κ (the x-axis labels of the inset act as a legend for the curves). Inset: each point is the average of 10 frames with $\rho = 2{,}300$ mm^{-2} for 3 different wells with 1 s.d. error bars.

polydimethylsiloxane (PDMS); this hemispherical structure has isotropic curvature everywhere on the surface, thus allowing us to isolate the effect of curvature on cell behaviour. Onto this PDMS substrate, we coated a layer of collagen I, and then cultured a monolayer of Madin–Darby canine kidney (MDCK) epithelial cells with stably expressed green fluorescent protein-tagged nuclear localization signal (NLS-GFP). After cell monolayers reached confluency, we imaged these cells in 3D every 15 min using confocal microscopy (SP8, Leica) (Fig. 1d,e and Supplementary Video 1; cross-sectional views are shown in Supplementary Fig. 2c); this allowed us to track cell positions over time, and then calculate migration velocities of each cell in 3D (Supplementary Fig. 1a–d). To avoid any boundary effect (Supplementary Fig. 1f,g), we excluded cells that were too close to the boundary of these hemispheres in our analysis (Methods).

Consistent with previous studies on flat surfaces[9], on these curved surfaces the average migration speed of individual cells decreased as cell density increased (Fig. 1f). We found that the dependence of individual cell speed on cell density did not vary with the magnitude of substrate curvature, whether positive or negative. To confirm this result, we quantified individual cell speed within a cell density (ρ) range of $2{,}300 \pm 300$ mm^{-2}; we found that cells had a similar speed on all tested curvatures (Supplementary Fig. 1e).

Intriguingly, even though individual cell speeds in this system were insensitive to curvature, collective behaviour responded dramatically to curvature. A standard way to quantify the degree of collectiveness is to compute the spatial cross-correlation function in the velocity field, $C_{vv}(r\theta, t_0) = \langle (\mathbf{v}(\mathbf{x}+\mathbf{r\theta}, t_0/|\mathbf{v}(\mathbf{x}+\mathbf{r\theta}, t_0)|) \cdot (\mathbf{v}(\mathbf{x}, t_0)/|\mathbf{v}(\mathbf{x}, t_0)|) \rangle$ (Methods), where $\boldsymbol{v}$ is velocity vector for cells in 3D and $\boldsymbol{x}$ is the position vector of cells in 3D, $r\theta$ is the geodesic distance for radius r and angle θ defined in Fig. 1c; this metric measures the velocity vector correlation of all cell pairs separated by a distance $r\theta$ at a certain time t_0. To avoid the influence of cell density on collective behaviour, we used the same cell

density (~2,300 mm^{-2}) on all hemispherical structures. For all curvatures examined, we observed that C_{vv} decreased as $r\theta$ increased (Fig. 1g), indicating that cells become less coherent with increased distance. Moreover, C_{vv} is always marked by a distinct minimum at intermediate distances; this is consistent with previous studies on flat surfaces, and indicates the existence of a swirling pattern of the collective cell migration with velocity vectors on the opposite side of the swirl being anticorrelated[22]. The correlation function invariably exhibits this well-defined minimum corresponding to the size of the swirls[22], and its position allowed us to determine a correlation length, ζ_0, characterizing the length scale of collective migration. Regardless of positive or negative curvatures, as the curvature magnitude increased, the correlation function decreased faster and reached a minimum at a shorter geodesic distance rθ, suggesting a smaller ζ_0 (inset in Fig. 1g). These results suggest that cell migration becomes less collective as surfaces become more curved. In contrast to cells cultured in tubes showing F-actin alignment along the tube direction[27,28], we observed no such change in F-actin or E-cadherin as isotropic curvature changed (Supplementary Fig. 3a,b). We also observed no obvious change in focal adhesion proteins such as vinculin (Supplementary Fig. 3d) and tight junction protein ZO-1 (Supplementary Fig. 3e). However, zyxin seemed to localize at cell–cell contacts for the higher curvature, whereas it was more cytoplasmic for flat or weakly curved substrates. This could be related to the observation that zyxin could relocalize from focal adhesions to actin filaments due to mechanical forces[31–33].

To further investigate collective cell migration on different curvatures, we decomposed the cell velocity field into divergence, curl and shear, which form a complete descriptor of a multicellular flow field (Methods). Divergence describes swelling and shrinking of cell clusters, while curl quantifies rotational motion and shear describes transvection, as illustrated in Supplementary Fig. 4a–c. As the spatial correlation of velocity directions is already captured by C_{vv} and ζ_0, here we only considered the magnitude of curl and shear. We found that divergence, curl and shear all had larger values but smaller characteristic pattern sizes on smaller hemispheres (Fig. 2a and Supplementary Fig. 4d,e,j–l). To quantify this trend, we plotted the probability density function (PDF) of divergence values calculated on every grid of a hemisphere (Methods); we found that the distribution of the PDF was wider on smaller hemispheres (Fig. 2d), indicating a more heterogenous system response. Additionally, as we plotted the divergence values along longitudinal lines on each hemisphere, we observed that the divergence values showed more pronounced fluctuations on smaller hemispheres (Fig. 2c). As we computed the spatial frequency spectrum of these fluctuations, we found a higher characteristic spatial frequency on smaller hemispheres (Fig. 2e), which confirmed the observed smaller patterns of the divergence field. Similar trends were also observed for curl and shear fields (Supplementary Fig. 4m–n). These results are also in agreement with the observed shorter velocity cross-correlation length on smaller hemispheres (inset in Fig. 1g). Taken together, these analyses of multicellular flow field demonstrate that collective migration of multicellular systems is strongly influenced by curvature in 3D; specifically, on smaller hemispheres with larger curvatures the collective cellular migration becomes less cooperative and less stable.

To test whether this curvature-dependent behaviour can be generalized to more physiologically relevant systems, we used the lung alveolospheres derived from human induced pluripotent stem cells (iPSCs) in 3D cell culture[34] (Fig. 3a). This alveolosphere system contained a monolayer of human iPSC-derived alveolar epithelial type II cells (iAEC2s) cultured in 3D Matrigel. These cells expressed a global transcriptome and ultrastructure that resembled primary adult alveolar epithelial type 2 cells, thus serving as a useful in vitro model of human lung development and diseases in these cells. In Matrigel, these alveolospheres undergo spontaneous expansion driven by continuous cell division, and maintain a spherical shape with an isotropic negative curvature on the surface (Fig. 3a). As the size of an alveolosphere increases, its surface curvature decreases (Fig. 3b), thus allowing us to investigate the impact of curvature on the behaviour of the constituted iAEC2s in these alveolospheres.

To visualize the structure and dynamics of cells in alveolospheres, we transfected these iAEC2s with a lentiviral vector to stably express NLS-GFP, and imaged the entire alveolosphere using confocal microscopy at a frame rate of 15 min per frame over 5 h (Fig. 3b and Supplementary Videos 2–7). We thus tracked the positions of individual cell nuclei and obtained their trajectories and velocities in 3D. Similar to the fabricated hemispheres, trajectories and velocities of individual iAEC2s on these spherical alveolospheres of different radii allowed us to calculate multicellular flow field components, including divergence, curl and shear, and compare them with values for alveolospheres with different curvatures (Fig. 3c).

Consistent with results on fabricated hemispheres, we observed more heterogeneous and more dynamic flow fields on smaller alveolospheres, where the PDFs of different flow field components were indeed more widely spread (Fig. 3d). To further quantify the characteristic size of these flow patterns, we identified local peak values and took the surrounding area with values above 50% of the local peak as a pack and measured the size of these packs (Supplementary Fig. 4g). We found that the average pack size decreased as the alveolosphere curvature increased (Fig. 3e and Supplementary Fig. 4h,i). These results show that the multicellular flow field of iAEC2s migration is more pronounced on smaller alveolospheres and becomes more collective, yet less dynamic, as alveolospheres grow larger.

Within epithelia, the shape of cells has been shown to be an important feature for understanding various normal and pathological processes[3,12,23,35,36]. Using nuclear positions in both cell systems, we obtained cell shapes and the cell–cell contact network in the live cell system by performing Voronoi tessellation (Supplementary Fig. 6a). By comparison with immunofluorescent staining on a fixed sample, we found that the Voronoi boundaries agreed reasonably with the actual cell boundaries; there was a slight underestimation on the cell shape index calculated from Voronoi tessellation because Voronoi tessellation has no edge tortuosity compared with the actual cell edges (Supplementary Fig. 6a,b). Previous analysis of animal tissues has shown a wide distribution of polygonal cell shapes, with hexagonal cell shape being the most frequent in simple epithelia[12,37], a topology commonly thought to reflect a tendency for cell sorting towards optimally packed (but nonetheless imperfect) honeycomb-like arrays[38]. Indeed, when we used Voronoi tessellation to examine cell–cell networks in alveolospheres, we found that cells with six neighbours also formed packs in all samples we examined (Fig. 4a) and they agreed reasonably well with the hexagon packs identified using cell boundaries (Supplementary Fig. 6c,d). To investigate the behaviour of these packs, we followed them over time and found that the constituent cells maintained their shape over the timescale of ~1 h (Supplementary Fig. 7a,b). The relative persistency of these cellular hexagon packs enabled the characterization of their sizes. When we measured the average size of the largest three packs on each alveolosphere, we found that the largest pack size increased as the alveolosphere expanded (Fig. 4a,f), suggesting that curvature sets a critical pack size for cell clustering. In addition, when we traced the shape of individual cells on different alveolospheres, we found that cell shapes became more persistent as alveolospheres grew bigger (Supplementary Fig. 7c,d). These results also suggest that cell groups on small spheres with large curvature surfaces are less stable, consistent with our flow field analyses.

To better understand the origin of the curvature-dependent behaviour of cells, we used numerical simulations to analyse the emergence of dynamic correlations in cell motion. Here we adapted the dynamic vertex model (DVM)[20,36] to model a confluent cell monolayer embedded on a spherical surface (see the Supplementary

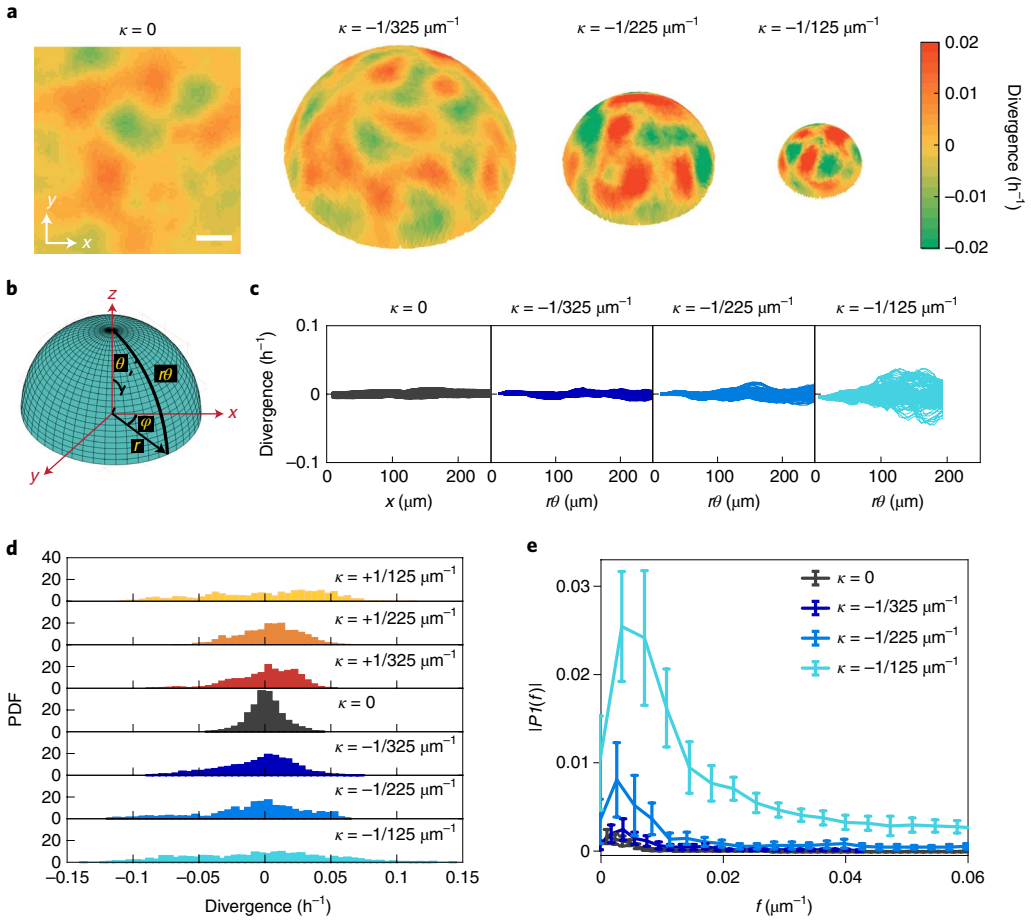

Fig. 2 | The multicellular flow field for MDCK cells is more dynamic with larger curvature. a, Divergence colour map on concave wells (flipped). Divergence describes the swelling and shrinking of cells; red represents sources and green represents sinks. Divergence values increase while the pattern size decreases as κ increases. Scale bar, 100 μm. **b**, Schematic showing the geodesic lines $r\theta$ and how we constructed the grids. **c**, Divergence along the longitudinal lines (every 2°) for concave wells of different κ. **d**, PDFs for cells on different κ. The PDFs spread wider as the magnitude of κ increases, regardless of whether it is positive or negative. **e**, Single-sided magnitude spectrum $|P1(f)|$ of divergence along $r\theta$ for concave wells, as a function of the spatial frequency f. The $|P1(f)|$ peak value shifts to right as κ increases. Each line is averaged over 10–20 consecutive frames (15 min per frame) for one representative well. Error bars shows 1 s.d.

Information for details). Commensurate with experimental observations, in the DVM we related the total number of cells to the radius of curvature of the spherical surface (R); that is $N = 4\pi R^2$ such that the curvature κ is represented by cell number N in the simulation: $\kappa = 1/R = \sqrt{4\pi/N}$. In this model, cells generate motile forces with a magnitude v_0 that propels the cell to move along the spherical surface. This motile force also serves as the source of active fluctuations in the DVM, which gives rise to an effective temperature $T \propto v_0^2$ (ref. [39]). Using the DVM, we first observed a velocity correlation profile that adopted a very similar shape to the experiments (Fig. 4b). The velocity correlation length grew as the curvature decreased (inset in Fig. 4b), in the same manner as our experimental observation (Fig. 1g). These results suggest that the cell motion becomes more cooperative for spheres with lower curvature. Indeed, the variation in the velocity correlation length is commonly associated with changes in cooperativity among individuals[22,40]. These results indicate that the spatial curvature plays a direct role in controlling collective behaviour of the cell monolayer.

Consistent with the experiments, in the DVM the hexagonal cells also tended to organize into large clusters (Fig. 4a), and the maximum size of these clusters N_c always increased as curvature was reduced. Furthermore, N_c decreased as the cell motility-driven T increased (Fig. 4e). These results suggest that cellular hexagon clusters are energetically favourable in the absence of other factors. To gain a physical insight into the clustering of hexagonal cells, we used a simple mean-field lattice gas Blume–Emery–Griffiths (BEG) model[41] to study the distribution of cells with different coordination numbers (see the Supplementary Information for details). Briefly, in the BEG model the hexagonal configuration is treated as the ground state for a cell while the non-hexagonal state is treated as an excited state. This is analogous to treating non-hexagonal cells as topological defects[42–44] inside a mostly crystalline (hexagonal) structure. This model predicted that the total fraction of hexagons $f_6(T, N)$ was dependent on the temperature as well as the total cell number and would increase when the curvature decreased. Additionally, f_6 decreased rapidly if the effective temperature was raised (Supplementary Fig. 8b). These predictions show excellent agreement with the DVM simulation (Supplementary Fig. 8a). The BEG model also gave a value of the Gibbs free energy difference between a hexagonal cell and a non-hexagonal cell:

$$\mu_{\mathrm{hex}}(T, N) = -\Delta + \beta^{-1} \log\left[\frac{2f_6}{1 - f_6}\right]. \quad (1)$$

Here, Δ is a positive constant that corresponds to the energy difference between a non-hexagonal cell and a hexagonal one. The

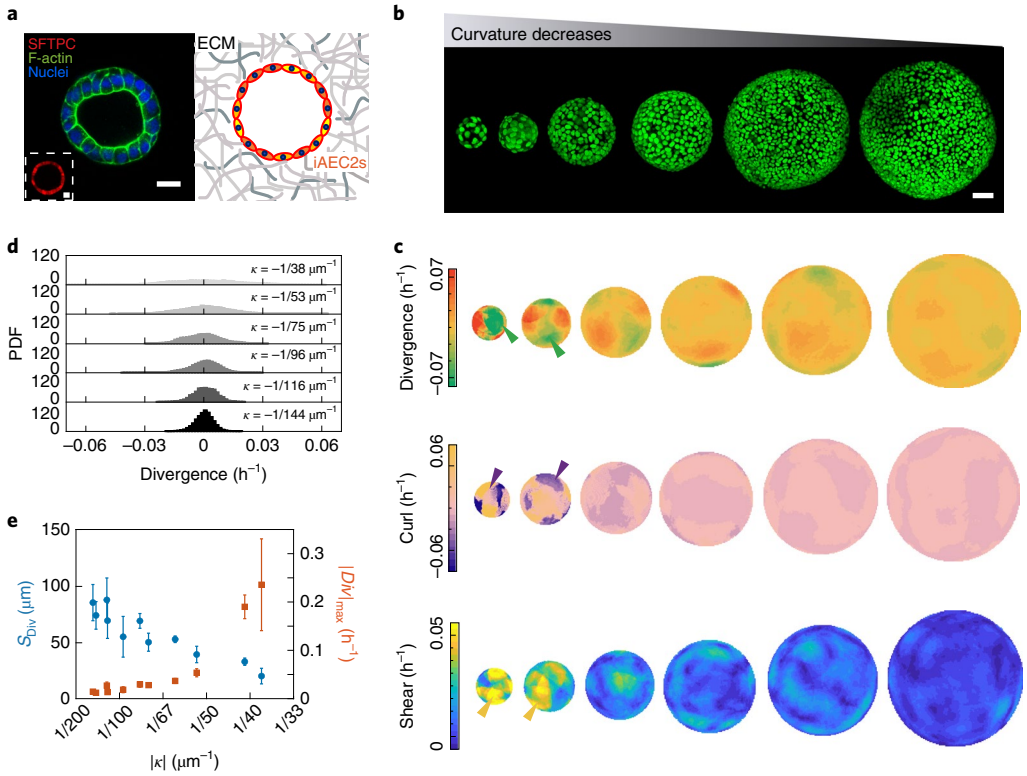

Fig. 3 | Alveolospheres derived from human iPSCs confirm that collective cellular behaviour is strongly affected by curvature. a, Left: Cross-sectional image of lung iAEC2s with F-actin (green) and nuclei (blue) and schematics of an alveolosphere cultured in 3D extracellular matrix. Left inset: alveolosphere with tdTomato targeted to the endogenous surfactant protein C (SFTPC) locus, suggesting a pure population of SFTPC-positive (SFTPC$^+$) iAEC2s. Right: Schematic figure of ECM and iAEC2s. Scale bars, 20 μm. **b**, *Z*-projection images of representative NLS-GFP-labelled (green) alveolospheres, ranging from 30 to 150 μm in radius. Scale bar, 50 μm. **c**, Multicellular flow field: divergence, curl, and shear colourmaps on different curvatures are shown. Arrows mark the highly dynamic regions. **d**, PDFs of divergence for representative alveolospheres. It spreads wider as the magnitude of κ increases. **e**, Divergence pattern size S_{Div} (the square root of the divergence pattern area) and peak value $|Div|_{max}$ as a function of absolute alveolosphere curvature. The peak divergence value increases while the pattern size decreases as curvature increases. Error bars were calculated from the s.d. over 10–20 consecutive frames (15 min per frame) for the same well. Each frame contains several hundred cells.

second term containing $\beta = 1/(k_B T)$ is the entropic (finite temperature) contribution to the Gibbs free energy, and k_B is the Boltzmann constant. Here μ_{hex} depends on T and N through $f_6(T, N)$. As μ_{hex} is negative for low temperatures, equation (1) confirms that hexagons are favoured and could suggest that these packs are more stable. Indeed, an overlay of the experimental flow field from the alveolosphere with the location of hexagonal clusters revealed that the highly dynamic flow field always occurred at the boundary of or outside hexagon clusters (Fig. 4c); the same trend was also observed in DVM (Fig. 4d). Therefore, cells that are part of a hexagonal pack are less dynamic compared with the 'bath' of cells outside these packs. To further test this conclusion, we measured the cell shape index in the DVM, a quantity that has successfully predicted the degree of fluidity of cells in flat cell layers[23,35]. The DVM shows that regardless of the spatial curvature, hexagonal cells are always more solid-like, while the non-hexagonal cells are fluid-like (Supplementary Fig. 8c). Interestingly, the stabilization of larger hexagonal clusters as curvature decreases is reminiscent of the nucleation and growth of crystals on curved surfaces[24,45–47], where the crystal must bend as it grows because it is constrained by the curvature of the surface. Adapting this concept of crystallization, our hypothesis here is that the less dynamic and more solid-like hexagonal cells would have a lower free energy and therefore may be regarded as a solid-like state analogous to a crystalline ground state. When hexagonal cells aggregate to form a cluster on a spherical surface, we expect a bending energy to arise due to deformation of the solid-like clusters. In contrast, no bending energy is incurred by the non-hexagonal cells due to their fluidity. Taken together, we can then write the total energy to form a circular hexagon pack[24]:

$$\Delta G(a) = \mu_{hex}\frac{\pi a^2}{4} + \frac{\pi}{24567}Y\frac{a^6}{R^4} \quad (2)$$

where a is the characteristic linear size of hexagon packs and Y is the 2D Young's modulus of the cell pack. By minimizing ΔG we obtain a critical pack size a_c as:

$$a_c = \sqrt[4]{-\frac{2048\mu_{hex}}{Y}}R \quad (3)$$

which is linearly proportional to R. Indeed, we found that the experimentally measured dependence of the largest hexagon pack size on alveolosphere radius was fitted well by a linear function (Fig. 4f). Furthermore, simulations showed that the linear relationship between N_c and N existed for a range of cell speeds (Fig. 4e); this linear relationship was expected and can be derived from equation (2) by taking an assumption used in the DVM simulation: $N = 4\pi R^2$. In addition, the largest hexagonal cluster size decreased as the effective temperature in DVM increased (Fig. 4e). This is explained by the theory prediction given by $\frac{N_c}{N} \propto \sqrt{-\mu_{hex}}$ where $|\mu_{hex}|$ decreases as T increases (Fig. 4e and Supplementary Fig. 8d); therefore, the formation of hexagonal clusters becomes less favourable as cell velocity

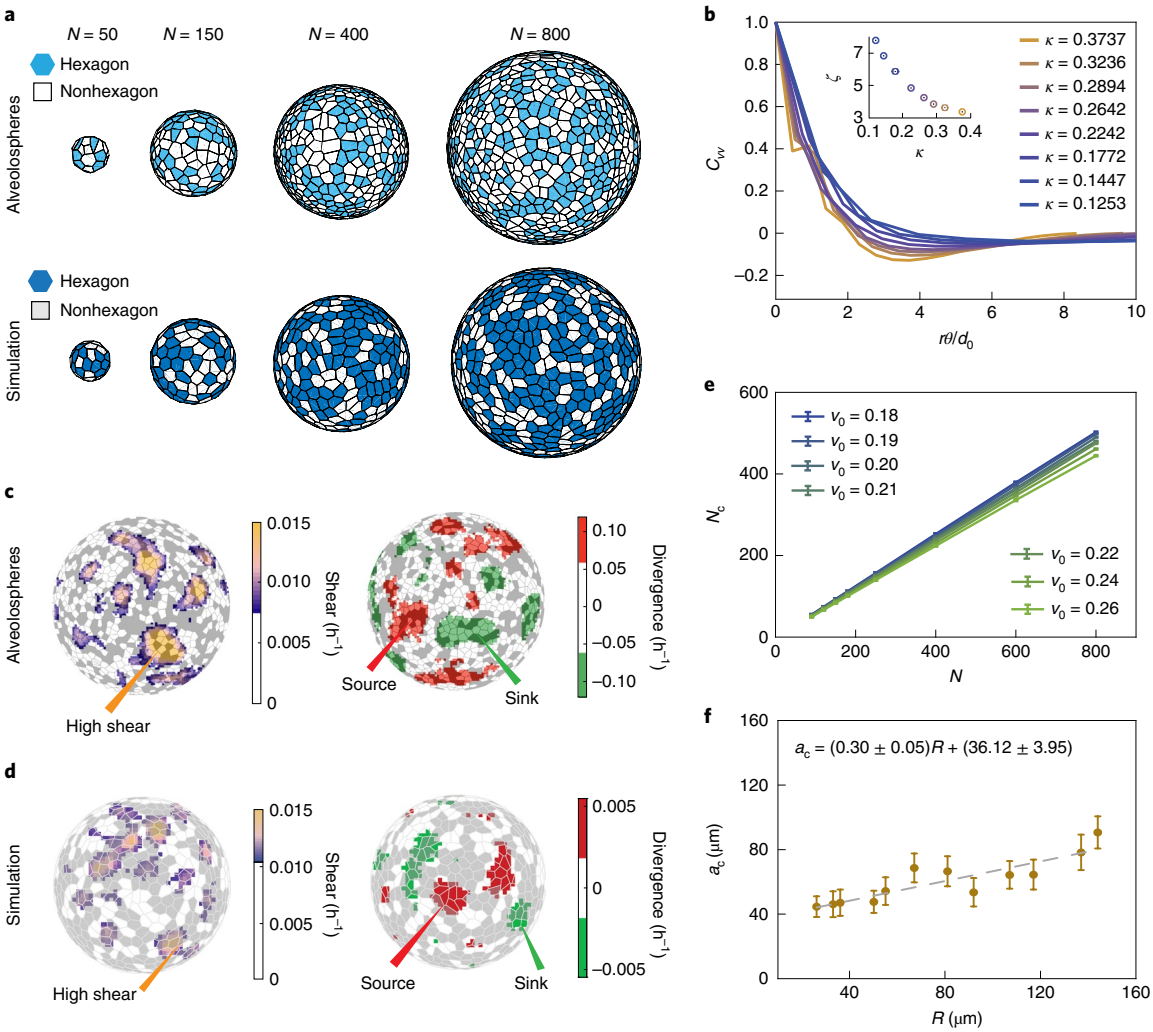

Fig. 4 | Curvature-induced bending energy causes higher dynamics in the multicellular flow field. a, Top: hexagon and non-hexagon packs on alveolospheres obtained using Voronoi tessellation. Bottom: hexagon and non-hexagon packs obtained by the DVM simulation. Both the simulation and experiment show that hexagons tend to form packs and isolate themselves from non-hexagons. **b**, C_{vv} as a function of geodesic distance normalized by cell size $r\theta/d_0$. Inset: ζ in terms of a series of curvatures in the DVM simulation; ζ was measured by the distance where correlation function reached the minimum. **c**,**d**, Overlays of the hexagon packs and the multicellular flow field (shear (left) and divergence (right)) in alveolospheres (**c**) and in the DVM simulation (**d**) show that highly dynamic flow occurs at the boundary of or outside the hexagon packs. Hexagons are shaded grey and non-hexagons are white. **e**, The DVM simulation shows that the critical hexagon pack size N_c (the square root of the largest hexagon pack area in each time frame) is linearly proportional to the total cell number over a wide velocity range. v_0 is a series of velocity magnitudes in simulation. **f**, Critical hexagon pack size a_c increases linearly with sphere radius R in alveolospheres. For each frame, the largest hexagon pack size was calculated as the average of the three largest hexagon packs. Dashed line shows a linear fitting of the largest hexagon pack size as a function of sphere radius R. Coefficient of determination = 0.79. Each dot and error bar in the plot represents the average and s.d. calculated from 10–20 consecutive frames (15 min per frame) in one alveolosphere of a certain size.

increases. This result confirms that the free energy difference fitted from $\Delta G(a)$ is reflective of a two-phase model in the alveolosphere system. Taken together, these results suggest that multicellular-scale curvature influences collective cell migration by introducing an elastic bending energy associated with the formation of hexagonal cell packs; this elastic energy penalty and free energy reduction associated with hexagonal cell pack formation compete to determine the critical pack size on different curvatures. For spheres that are small, the elastic bending energy is high and as a result the formation of hexagon clusters is supressed. As hexagons have a lower free energy, their suppression leads to a more unstable monolayer. We thus observe less collective cell migration, a stronger multicellular flow field and more dynamic multicellular flow patterns as curvature increases.

Discussion

Using MDCK cells on fabricated hemispherical geometries and human iPSC-derived lung alveolospheres in 3D, we demonstrate that curvature plays a pivotal role in regulating collective cell migration. Unlike nano-scale[26] and single-cell-scale[48,49] curvature sensing, multicellular-scale curvature sensing in cell monolayers is achieved through not an individual, but instead a collective, manner. For example, we did not observe obvious changes in the single-cell speed and height, F-actin cytoskeleton, or adhesion and junction proteins (Supplementary Figs. 1e, 2 and 3). Instead, cells on large curvatures reduce their collectiveness and demonstrate highly dynamic multicellular flow, owing to the fact that the cells bear a larger elastic bending energy when forming solid-like hexagonal packs. This bending energy has also been previously acknowledged

when highly curved curls form spontaneously at the free edge of epithelial monolayers devoid of substrate in vivo and in vitro[50,51]. Furthermore, when we linearly extrapolated the relationship between correlation length and curvature to a single-cell size, we found a critical curvature radius where collectivity disappears, at about 9 to 10 cell lengths in both systems (Supplementary Fig. 9); this critical curvature may represent an intrinsic characteristic of multicellular-scale curvature sensing. Our results also suggest that cells sense the inherent curvature of the monolayer, instead of the curvature of the substrate: we found that collective cell migration responded to the magnitude of substrate curvature in the same fashion regardless of whether the surface was concave or convex.

Our numerical simulation and the mean-field model were successful in capturing the velocity correlations during multicellular migration. They also provided a quantitative explanation for the curvature-dependent organization of hexagonal cellular packs. These theoretical methods apply to cells moving on the spherical surface, which has a constant Gaussian curvature. To fully appreciate the role of substrate curvature in directing multicellular behaviour it will be necessary to extend these ideas to cells constrained on cylindrical or other non-spherical curved substrates. This would involve modifications to the BEG model and equation (2), where the energy terms for forming hexagonal packs are dependent on the local geometry and the orientation of the pack with respect to the local principal curvatures. It would also be informative to conduct further experimental measurements to investigate the mechanics and bending energy difference of hexagons compared with non-hexagons on curved surfaces.

Although we focused on collective cellular migration, our study raises questions about the broader impact that curvature may have on a variety of functional and morphological behaviours, such as cell packing during development. For example, in *Drosophila* morphogenesis the cell shape change and cell alignment become obvious during ventral furrow folding, where the tissue curvature changes dramatically[23,52]. This indicates a strong correlation between cell packing and curvature that remains to be explored. Besides proposing a new perspective on understanding lung alveolosphere expansion, the universal understanding showed here could be applied to many multicellular systems, such as embryonic development and cancer invasion. Evidence has shown that positive or negative tissue curvature is related to two types of tumour neoplastic growth morphogenesis[53], yet a more detailed biophysics understanding of how curvature causes the different morphology is still lacking.

Online content

Any methods, additional references, Nature Research reporting summaries, source data, extended data, supplementary information, acknowledgements, peer review information; details of author contributions and competing interests; and statements of data and code availability are available at https://doi.org/10.1038/s41567-022-01747-0.

Received: 15 July 2021; Accepted: 5 August 2022;
Published online: 3 October 2022

References

1. Aoki, K. et al. Propagating wave of ERK activation orients collective cell migration. *Dev. Cell* **43**, 305–317 (2017).
2. Barriga, E. H., Franze, K., Charras, G. & Mayor, R. Tissue stiffening coordinates morphogenesis by triggering collective cell migration in vivo. *Nature* **554**, 523–527 (2018).
3. Wang, X. et al. Anisotropy links cell shapes to tissue flow during convergent extension. *Proc. Natl Acad. Sci. USA* **117**, 3541–1355 (2020).
4. Brugués, A. et al. Forces driving epithelial wound healing. *Nat. Phys.* **10**, 683–690 (2014).
5. Ajeti, V. et al. Wound healing coordinates actin architectures to regulate mechanical work. *Nat. Phys.* **15**, 696–705 (2019).
6. Levental, K. R. et al. Matrix crosslinking forces tumor progression by enhancing integrin signaling. *Cell* **139**, 891–906 (2009).
7. Han, Y. L. et al. Cell swelling, softening and invasion in a three-dimensional breast cancer model. *Nat. Phys.* **16**, 101–108 (2019).
8. Trepat, X. et al. Physical forces during collective cell migration. *Nat. Phys.* **5**, 426–430 (2009).
9. Angelini, T. E. et al. Glass-like dynamics of collective cell migration. *Proc. Natl Acad. Sci. USA* **108**, 4714–4719 (2011).
10. Serra-Picamal, X. et al. Mechanical waves during tissue expansion. *Nat. Phys.* **8**, 628–634 (2012).
11. Bi, D., Lopez, J. H., Schwarz, J. M. & Manning, M. L. Energy barriers and cell migration in densely packed tissues. *Soft Matter* **10**, 1885–1890 (2014).
12. Gibson, M. C., Patel, A. B., Nagpal, R. & Perrimon, N. The emergence of geometric order in proliferating metazoan epithelia. *Nature* **442**, 1038–1041 (2006).
13. Farhadifar, R., Röper, J.-C., Aigouy, B., Eaton, S. & Jülicher, F. The influence of cell mechanics, cell-cell interactions, and proliferation on epithelial packing. *Curr. Biol.* **17**, 2095–2104 (2007).
14. Wyatt, T. P. et al. Emergence of homeostatic epithelial packing and stress dissipation through divisions oriented along the long cell axis. *Proc. Natl Acad. Sci. USA* **112**, 5726–5731 (2015).
15. Ramanathan, S. P., Krajnc, M. & Gibson, M. C. Cell-size pleomorphism drives aberrant clone dispersal in proliferating epithelia. *Dev. Cell* **51**, 49–61 (2019).
16. Mongera, A. et al. A fluid-to-solid jamming transition underlies vertebrate body axis elongation. *Nature* **561**, 401–405 (2018).
17. Palamidessi, A. et al. Unjamming overcomes kinetic and proliferation arrest in terminally differentiated cells and promotes collective motility of carcinoma. *Nat. Mater.* **18**, 1252–1263 (2019).
18. Yan, L. & Bi, D. Multicellular rosettes drive fluid-solid transition in epithelial tissues. *Phys. Rev. X* **9**, 011029 (2019).
19. Ilina, O. et al. Cell–cell adhesion and 3D matrix confinement determine jamming transitions in breast cancer invasion. *Nat. Cell Biol.* **22**, 1103–1115 (2020).
20. Mitchel, J. A. et al. In primary airway epithelial cells, the unjamming transition is distinct from the epithelial-to-mesenchymal transition. *Nat. Commun.* **11**, 5053 (2020).
21. Petridou, N. I., Corominas-Murtra, B., Heisenberg, C.-P. & Hannezo, E. Rigidity percolation uncovers a structural basis for embryonic tissue phase transitions. *Cell* **184**, 1914–1928 (2021).
22. Angelini, T. E., Hannezo, E., Trepat, X., Fredberg, J. J. & Weitz, D. A. Cell migration driven by cooperative substrate deformation patterns. *Phys. Rev. Lett.* **104**, 168104 (2010).
23. Atia, L. et al. Geometric constraints during epithelial jamming. *Nat. Phys.* **14**, 613–620 (2018).
24. Meng, G., Paulose, J., Nelson, D. R. & Manoharan, V. N. Elastic instability of a crystal growing on a curved surface. *Science* **343**, 634–637 (2014).
25. Guerra, R. E., Kelleher, C. P., Hollingsworth, A. D. & Chaikin, P. M. Freezing on a sphere. *Nature* **554**, 346–350 (2018).
26. Zhao, W. et al. Nanoscale manipulation of membrane curvature for probing endocytosis in live cells. *Nat. Nanotechnol.* **12**, 750 (2017).
27. Yevick, H. G., Duclos, G., Bonnet, I. & Silberzan, P. Architecture and migration of an epithelium on a cylindrical wire. *Proc. Natl Acad. Sci. USA* **112**, 5944–5949 (2015).
28. Xi, W., Sonam, S., Saw, T. B., Ladoux, B. & Lim, C. T. Emergent patterns of collective cell migration under tubular confinement. *Nat. Commun.* **8**, 1517 (2017).
29. Harmand, N., Huang, A. & Hénon, S. 3D shape of epithelial cells on curved substrates. *Phys. Rev. X* **11**, 031028 (2021).
30. Luciano, M. et al. Cell monolayers sense curvature by exploiting active mechanics and nuclear mechanoadaptation. *Nat. Phys.* **17**, 1382–1390 (2021).
31. Yoshigi, M., Hoffman, L. M., Jensen, C. C., Yost, H. J. & Beckerle, M. C. Mechanical force mobilizes zyxin from focal adhesions to actin filaments and regulates cytoskeletal reinforcement. *J. Cell Biol.* **171**, 209–215 (2005).
32. Winkelman, J. D., Anderson, C. A., Suarez, C., Kovar, D. R. & Gardel, M. L. Evolutionarily diverse LIM domain-containing proteins bind stressed actin filaments through a conserved mechanism. *Proc. Natl Acad. Sci. USA* **117**, 25532–25542 (2020).
33. Rosner, S. R. et al. The actin regulator zyxin reinforces airway smooth muscle and accumulates in airways of fatal asthmatics. *PLoS ONE* **12**, e0171728 (2017).
34. Jacob, A. et al. Differentiation of human pluripotent stem cells into functional lung alveolar epithelial cells. *Cell Stem Cell* **21**, 472–488 (2017).
35. Park, J.-A. et al. Unjamming and cell shape in the asthmatic airway epithelium. *Nat. Mater.* **14**, 1040–1048 (2015).
36. Das, A., Sastry, S. & Bi, D. Controlled neighbor exchanges drive glassy behavior, intermittency, and cell streaming in epithelial tissues. *Phys. Rev. X* **11**, 041037 (2021).

37. Schwann, T. *Microscopical Researches into the Accordance in the Structure and Growth of Animals and Plants* (Sydenham Society, 1847).
38. Thompson, D. W. & Thompson, D. A. W. *On growth and form* (Cambridge Univ. Press, 1942).
39. Bi, D., Yang, X., Marchetti, M. C. & Manning, M. L. Motility-driven glass and jamming transitions in biological tissues. *Phys. Rev. X* **6**, 021011 (2016).
40. Olsson, P. & Teitel, S. Critical scaling of shear viscosity at the jamming transition. *Phys. Rev. Lett.* **99**, 178001 (2007).
41. Blume, M., Emery, V. J. & Griffiths, R. B. Ising model for the λ transition and phase separation in He^3-He^4 mixtures. *Phys. Rev. A* **4**, 1071 (1971).
42. Flegg, G. *From Geometry to Topology* 1st edn (Dover, 2001).
43. Bowick, M., Cacciuto, A., Nelson, D. R. & Travesset, A. Crystalline order on a sphere and the generalized Thomson problem. *Phys. Rev. Lett.* **89**, 185502 (2002).
44. Chaikin, P. M. & Lubensky, T. C. *Principles of Condensed Matter Physics* (Cambridge Univ. Press, 1995).
45. Gómez, L. R., García, N. A., Vitelli, V., Lorenzana, J. & Vega, D. A. Phase nucleation in curved space. *Nat. Commun.* **6**, 6856 (2015).
46. Brojan, M., Terwagne, D., Lagrange, R. & Reis, P. M. Wrinkling crystallography on spherical surfaces. *Proc. Natl Acad. Sci. USA* **112**, 14–19 (2015).
47. Azadi, A. & Grason, G. M. Neutral versus charged defect patterns in curved crystals. *Phys. Rev. E* **94**, 013003 (2016).
48. Pieuchot, L. et al. Curvotaxis directs cell migration through cell-scale curvature landscapes. *Nat. Commun.* **9**, 3995 (2018).
49. Chen, T. et al. Large-scale curvature sensing by directional actin flow drives cellular migration mode switching. *Nat. Phys.* **15**, 393–402 (2019).
50. Fouchard, J. et al. Curling of epithelial monolayers reveals coupling between active bending and tissue tension. *Proc. Natl Acad. Sci. USA* **117**, 9377–9383 (2020).
51. Wyatt, T. P. et al. Actomyosin controls planarity and folding of epithelia in response to compression. *Nat. Mater.* **19**, 109–117 (2020).
52. Yevick, H. G., Miller, P. W., Dunkel, J. & Martin, A. C. Structural redundancy in supracellular actomyosin networks enables robust tissue folding. *Dev. Cell* **50**, 586–598 (2019).
53. Messal, H. A. et al. Tissue curvature and apicobasal mechanical tension imbalance instruct cancer morphogenesis. *Nature* **566**, 126–130 (2019).

Publisher's note Springer Nature remains neutral with regard to jurisdictional claims in published maps and institutional affiliations.

Springer Nature or its licensor holds exclusive rights to this article under a publishing agreement with the author(s) or other rightsholder(s); author self-archiving of the accepted manuscript version of this article is solely governed by the terms of such publishing agreement and applicable law.

© The Author(s), under exclusive licence to Springer Nature Limited 2022

Methods

Fabrication of PDMS hemispheres. Glass beads (Polysciences) with three diameter ranges, 200–300 μm, 420–500 μm and 600–700 μm, were placed on clean silicon wafers and a layer of SU-8 2000 with the thickness of roughly the radius of beads was subsequently applied using soft lithography to obtain the hemispherical shapes. Briefly, we exposed a SU-8 2000 photoresist to a conventional UV radiation with wavelength in the range of 350–400 nm. Upon exposure, cross-linking proceeds in two steps: (1) the formation of a strong acid during the exposure step, followed by (2) acid-catalysed, thermally driven epoxy cross-linking during the post exposure bake step. As a result, the beads with different sizes are fixed onto the silicon wafers. Then PDMS (SYLGARD 184 silicon elastomer base) and cross-linker (SYLGARD 184 silicon elastomer curing agent) (volume 10:1) were mixed together following a well-established method and placed in a vacuum chamber to get rid of the bubbles at room temperature. A thin PDMS layer (~3 mm) was poured onto the fabricated silicon wafer. The sample was placed into a 60 °C constant-temperature oven (Thermo Scientific) overnight to cure into an elastomer. Concave PDMS wells with different diameters can be obtained by peeling the PDMS layer off the silicon wafer. Convex geometries were made by fixing glass beads inside a very thin PDMS layer, followed by the same procedures.

MDCK cells and iAEC2 cluster culture. Before seeding cells, a 0.1 mg ml^{-1} collagen solution (diluted in 1× PBS, Advanced BioMatrix) was coated onto the surfaces of wells overnight in a refrigerator at 4 °C. We then placed the MDCK cells (ATCC) on the precoated PDMS. MDCK cells were cultured in DMEM medium (Corning), supplemented with 10% fetal bovine serum (ATCC) and 1% penicillin-streptomycin (ThermoFisher). To subculture cells, a 0.25% Trypsin-EDTA solution (Corning) was used to detach and separate cells. After neutralizing with culture medium, the cell suspensions were then centrifuged at 800 r.p.m. for 5 min. After pouring the liquid out, 5 ml complete culture medium was added and pipetted several times to fully mix and separate cells.
The cell solutions were then ready to use. The PDMS geometries were first pressed onto the bottom of 35 mm petri dishes. Then one droplet of the cell solution was added to each small PDMS sheet; the sheets were then put into incubator for 1 h to allow cells to attach to the PDMS substrate. Then 2–3 ml of the complete culture medium was added into each petri dish. MDCK cells formed confluent monolayer after 2–3 days under 5% CO_2 at 37 °C in a humidified incubator.

iAEC2s with a tdTomato reporter targeted to the endogenous surfactant protein C (SFTPC) locus (SPC2-SFTPC^{tdTomato}-B2 line) were generated via directed differentiation as previously described[34,54]. SFTPC$^+$ cells were maintained in 3D Matrigel (Corning) as alveolospheres at 400 cells μl^{-1} Matrigel, and passaged every 10–14 days. A lentiviral vector with constitutively and ubiquitously active long EF1a promoter (EF1aL) driving the expression of nuclear localized GFP (nlsGFP) was engineered by cloning an NLS in front of GFP. The resulting construct (pHAGE EF1aL-nlsGFP-W) with full plasmid map and sequence is available from Addgene (plasmid no. 126688). Lentiviral infection of iAEC2s was performed in suspension culture at a multiplicity of infection of 20, as previously detailed[54], and NLS-GFP-expressing cells were purified by a subsequent culture passage through fluorescence-activated cell sorting and replated for serial sphere passaging in 3D culture. For imaging, NLS-GFP-expressing iAEC2s were seeded in 3D Matrigel droplets in 35 mm glass-bottom petri dishes at 100 cells μl^{-1}. These cells would naturally grow into alveolospheres in 3D driven by spontaneous cell division. As these alveolospheres grew bigger, the cell layer thickness remained nearly constant (Supplementary Fig. 2b), while the cell number density changed (Supplementary Fig. 5a).

The boundary condition of MDCK cells on hemispheres. For PDMS wells, the place where the curved surface and flat surface meet creates a boundary. To check for potential boundary effects in our analysis, we calculated the mean squared displacement of cells near the boundary and compared to the mean squared displacement of cells near the centre of a well as shown in Supplementary Fig. 1. We found that there was no obvious difference in the mean squared displacement of cells near the boundary versus those at the centre. However, a boundary did affect the divergence, curl and shear calculations, as we needed a kernel radius to obtain an average; the value at the boundary was averaged among fewer pixels, which may introduce some error. Therefore, we only used the data for cells that were far from boundaries in the PDMS wells. An effective boundary region could be defined as the correlation length that we calculated for different curvatures. We then avoided using the data in such boundary regions.

Cell density changes in alveolospheres. Unlike that for MDCK cells on fabricated wells, the cell density of alveolospheres cannot be externally controlled. There is an increase in density as a function of sphere radius r (Supplementary Fig. 5a), especially when $r < 100$ μm. To determine whether the increase in cell density had an effect on the collectiveness and pack size, we selected $r > 100$ μm where the cell density remained constant. When the cell density was constant, the velocity correlation and correlation length showed the same trend as MDCK cells on fabricated PDMS wells (Supplementary Fig. 5b). To test the effect of density change on divergence, curl and shear pack size N_{hexmax}, we used the fabricated well data to control the curvature to be the same while changing only the cell density. This showed that there was no obvious divergence, curl and shear pack size change as density increased (Supplementary Fig. 5c,d). Similarly, there was also no obvious change in terms of the largest hexagon pack size when density increased. Therefore, we concluded that cell density does not play a role in determining the trend we observed in collectiveness, hexagon pack size and multicellular fluidity in alveolospheres.

Cell layer thickness of MDCK cells and alveolospheres. Cell layer thickness was measured from the confocal fluorescent images for MDCK cells and bright-field images for alveolospheres. For MDCK cells, both F-actin and cell nuclei were fluorescently labelled, indicating the top and bottom of the cell, respectively. For alveolospheres, cell height was directly measured from the bright-field images of cross-sections.

Immunofluorescence staining. For immunohistochemical staining, the MDCK cell confluent monolayers on different curvatures were first washed with 1× PBS and then fixed with 4% formaldehyde at room temperature for 30 min, then rinsed three times in 1× PBS for 5 min each. To block the cells, the cell layers were immersed in blocking buffer composed of 1× PBS supplied with 0.3% Triton X-100 and 3% BSA (Cell Signaling). While blocking, primary antibody was diluted (1:200) inside in antibody dilution buffer, which is composed of 1× PBS with 1% BSA (Cell Signaling) and 0.3% Triton X-100. The sample was then covered with diluted primary antibody and incubated overnight at 4 °C. The corresponding secondary antibody diluted in antibody dilution buffer (1:350) was added for 2 h at room temperature in the dark. E-cadherin (24E10) rabbit monoclonal antibody no. 3195 (primary) and Alexa Fluor 568 goat anti-rabbit IgG (H + L) (secondary) were used for E-cadherin; ZO-1 monoclonal antibody (Invitrogen) (primary) and anti-rabbit Igg (H + L) (secondary) were used for ZO-1; Anti-zyxin developed in rabbit (Sigma-Aldrich) (primary) and CF568 (Sigma-Aldrich) (secondary) were used for zyxin; anti-vinculin mouse monoclonal antibody (Sigma-Aldrich) (primary) and anti-mouse-Igg - ATTO 647 antibody (Sigma-Aldrich) (secondary) were used for vinculin. To stain F-actin, samples were immersed in Phalloidin 633 nm (1:400 diluted in 1× PBS) for 1 h. To stain cell nuclei, DAPI (ThermoFisher) was added for 4 h. After each step, the samples were washed with PBS three times for 5 min each.

Image acquisition. To visualize the cell nuclei, cells with NLS-GFP were used. During imaging, MDCK cells grown on PDMS substrate were cultured in a 35 mm petri dish in a customized incubator (5% CO_2, 37 °C, 95% humidity) on a confocal microscope (Leica, TCL SP8). The images were taken every 15 min in 3D for ~8–12 h for MDCK cells and alveolospheres. A ×10/0.4 numerical aperture air objective, a ×25/0.95 numerical aperture water objective and a ×63/1.20 numerical aperture water objective were all used for imaging. Confocal microscopy was used to record the cell nuclear positions in 3D over time. Cell nuclear positions were then tracked using the Trackmate plugin in Fiji (2.3.0/1.53q). Immunofluorescence images were taken by a ×25/0.95 numerical aperture water objective. Imaging of alveolospheres and analyses was performed using the same method.

Correlation and correlation length. To calculate 3D spatial velocity correlation, we first moved one velocity vector along the geodesic line to the same coordinate as the other velocity vector. Then velocity cross-correlation was calculated as a function of $r\theta$ by $C_{vv}(r\theta, t_0) = \langle (\mathbf{v}(\mathbf{x}+\mathbf{r\theta}, t_0)/|\mathbf{v}(\mathbf{x}+\mathbf{r\theta}, t_0)|) \cdot (\mathbf{v}(\mathbf{x}, t_0)/|\mathbf{v}(\mathbf{x}, t_0)|) \rangle$ at a certain time t_0, where the angle brackets signify an average over all velocity vector positions $\mathbf{x}$. Because cell density can change over time, we chose a particular density (~2,300 mm^{-2}) for calculating C_{vv} when comparing curvatures. Correlation length was defined as the distance where the correlation function reaches the first minimum and each data point was calculated by an average of at least five datasets.

Grid generation for spheres. Grids were divided first in spherical coordinates $\Delta\theta = \Delta\varphi = \frac{8}{r} \cdot \frac{180}{\pi}$ in units of degrees to make sure that the grids had the same size for spheres of different sizes. Therefore, $\Delta\varphi_{r=125\,\mu m} = \Delta\theta_{r=125\mu m} = 3.67°$, $\Delta\varphi_{r=225\,\mu m} = \Delta\theta_{r=225\,\mu m} = 2.04°$,... Then the spherical coordinates were converted to Cartesian coordinates. A schematic of how the grids were divided is shown in Fig. 2b.

Decomposition of the velocity field. The velocity field in 3D can be decomposed into:

$$\mathbf{v}(\mathbf{r}+\mathbf{d}\,\mathbf{r}) = \mathbf{v}(\mathbf{r}) + \begin{bmatrix} \frac{\partial u}{\partial x} & 0 & 0 \\ 0 & \frac{\partial v}{\partial y} & 0 \\ 0 & 0 & \frac{\partial w}{\partial z} \end{bmatrix} \begin{bmatrix} \mathrm{d}x \\ \mathrm{d}y \\ \mathrm{d}z \end{bmatrix} + \begin{bmatrix} 0 & \frac{1}{2}\left(\frac{\partial u}{\partial y} - \frac{\partial v}{\partial x}\right) & \frac{1}{2}\left(\frac{\partial u}{\partial z} - \frac{\partial w}{\partial x}\right) \\ \frac{1}{2}\left(-\frac{\partial u}{\partial y} + \frac{\partial v}{\partial x}\right) & 0 & \frac{1}{2}\left(\frac{\partial v}{\partial z} - \frac{\partial w}{\partial y}\right) \\ \frac{1}{2}\left(-\frac{\partial u}{\partial z} + \frac{\partial w}{\partial x}\right) & \frac{1}{2}\left(-\frac{\partial v}{\partial z} + \frac{\partial w}{\partial y}\right) & 0 \end{bmatrix} \begin{bmatrix} \mathrm{d}x \\ \mathrm{d}y \\ \mathrm{d}z \end{bmatrix} + \begin{bmatrix} 0 & \frac{1}{2}\left(\frac{\partial u}{\partial y} + \frac{\partial v}{\partial x}\right) & \frac{1}{2}\left(\frac{\partial u}{\partial z} + \frac{\partial w}{\partial x}\right) \\ \frac{1}{2}\left(\frac{\partial u}{\partial y} + \frac{\partial v}{\partial x}\right) & 0 & \frac{1}{2}\left(\frac{\partial v}{\partial z} + \frac{\partial w}{\partial y}\right) \\ \frac{1}{2}\left(\frac{\partial u}{\partial z} + \frac{\partial w}{\partial x}\right) & \frac{1}{2}\left(\frac{\partial v}{\partial z} + \frac{\partial w}{\partial y}\right) & 0 \end{bmatrix} \begin{bmatrix} \mathrm{d}x \\ \mathrm{d}y \\ \mathrm{d}z \end{bmatrix} + O((d\mathbf{r})^2) \tag{4}$$

where $\mathbf{r} = (x, y, z)$ and $\mathbf{v} = (u, v, w)$. We defined the magnitude of div, curl and shear based on the velocity decomposition, and they are shown in the following equations:

$$\mathrm{div}\,(x, y, z, t) = \frac{\partial u(x,y,z,t)}{\partial x} + \frac{\partial v(x,y,z,t)}{\partial y} + \frac{\partial w(x,y,z,t)}{\partial z} \tag{5}$$

$$\mathrm{curl}\,(x, y, z, t) = \pm\sqrt{\left(\frac{\partial w(x,y,z,t)}{\partial y} - \frac{\partial v(x,y,z,t)}{\partial z}\right)^2 + \left(-\frac{\partial w(x,y,z,t)}{\partial x} + \frac{\partial u(x,y,z,t)}{\partial z}\right)^2 + \left(-\frac{\partial u(x,y,z,t)}{\partial y} + \frac{\partial v(x,y,z,t)}{\partial x}\right)^2} \tag{6}$$

$$\mathrm{shear}\,(x, y, z, t) = \sqrt{\left(\frac{\partial w(x,y,z,t)}{\partial y} + \frac{\partial v(x,y,z,t)}{\partial z}\right)^2 + \left(\frac{\partial w(x,y,z,t)}{\partial x} + \frac{\partial u(x,y,z,t)}{\partial z}\right)^2 + \left(\frac{\partial u(x,y,z,t)}{\partial y} + \frac{\partial v(x,y,z,t)}{\partial x}\right)^2} \tag{7}$$

We defined curl to be positive when the angle between $\nabla\times\boldsymbol{v}$ and the local outer radial direction is less than 90°, where $\nabla\times\boldsymbol{v}$ is the vorticity corresponding to the anti-symmetric part of the velocity gradient. Divergence, curl and shear convey useful information for describing the multicellular flow field. For each grid on hemispheres, the calculation was done on the tangential small area of the grid (that is, locally assuming the curved surface as a small flat surface). Cells that were used to calculate each grid were found within a ring of the kernel radius. For flat surfaces, the kernel ring radius was set to be 70 μm (±30 μm) to avoid single-cell fluctuations[55]. For curved surfaces, the kernel ring radius was set to be 50 μm (±20 μm). Next, divergence, curl and shear for each cell within the kernel ring were computed from the first-order derivatives of the flow at every grid (x, y, z) for every frame. The local divergence, curl and shear for each grid were obtained by averaging the values for all cells within the kernel ring. The divergence, curl and shear pattern sizes were defined as the top 50% of the peak or valley values. In each frame, these sizes were calculated by averaging the pattern sizes of the top three peaks. In the main text, a stronger multicellular flow field refers to a higher strength of divergence, curl and shear, which were defined as max $\{|\mathrm{div}_{\max}|, |\mathrm{div}_{\min}|\}$, max $\{|\mathrm{curl}_{\max}|, |\mathrm{curl}_{\min}|\}$ and max $\{|\mathrm{shear}_{\max}|, |\mathrm{shear}_{\min}|\}$, respectively.

Voronoi tessellation. Voronoi tessellation was performed on a unit sphere by projecting cell positions onto the unit sphere without changing the relative positions.

Cell shape index. In both the DVM simulations and experimental images, the cell shape index $q = \langle p/\sqrt{a}\rangle$ was computed by taking the average over all cells. The perimeter of a cell was obtained by summing the spherical arc lengths of all edges adjacent to it. The area of the cell was the area of the spherical polygon subtended by it.

Statistics. For comparison between multiple groups, single-factor ANOVA tests and non-parametric Kruskal–Wallis tests were performed using Excel. The non-parametric Kendall's tau test was performed to determine whether there were correlations between two parameters.

Reporting summary. Further information on research design is available in the Nature Research Reporting Summary linked to this article.

Data availability

The data that support the findings are available from the corresponding author upon reasonable request. Source data are provided with this paper.

Code availability

MATLAB scripts used in this paper are available from the corresponding author guom@mit.edu upon reasonable request.

References

54. Jacob, A. et al. Derivation of self-renewing lung alveolar epithelial type II cells from human pluripotent stem cells. *Nat. Protoc.* **14**, 3303–3332 (2019).
55. Zehnder, S. M. et al. Multicellular density fluctuations in epithelial monolayers. *Phys. Rev. E* **92**, 032729 (2015).

Acknowledgements

We acknowledge support from National Institute of General Medical Sciences grant number 1R01GM140108 and MathWorks. M.G. and D.B. are supported by the Sloan Research Fellowship. A.F.P. acknowledges NSERC Discovery and NSERC CRD grants to A. Stolow, the NRC-uOttawa Joint Centre for Extreme Photonics and the Max-Planck-University of Ottawa Centre for Extreme and Quantum Photonics. J.F. acknowledge supports from NHLBI under grant numbers 1R01HL148152 and PO1HL120839. D.N.K. acknowledge support from NIH grant numbers U01HL148692, U01HL134745, U01HL134766 and R01HL095993. iPSC distribution is supported by NIH grant numbers U01TR001810 and N01 75N92020C00005. A.D. and D.B. acknowledge support from the Northeastern University TIER 1 Grant and the Northeastern University Discovery Cluster, and the National Science Foundation DMR-2046683. A.D. also acknowledges support from the Centre for Theoretical Biological Physics at Northeastern University. We also thank C. Deng for helping plot the schematics figures in Fig. 1a,b.

Author contributions

W.T. and M.G. designed the experiments. M.G. supervised the project. W.T., J.H., D.A.R., Y.L.H. and H.Y. performed the experiments. W.T. analysed the experimental data. W.T., Y.L.H., A.D. and D.B. developed the MATLAB scripts for image processing and data analysis. A.D. and D.B. performed the simulation. W.T., A.F.P., A.D., J.J.F., D.N.K., D.B. and M.G. wrote the manuscript. All authors edited and approved the manuscript.

Competing interests

The authors declare no competing interests.

Additional information

Supplementary information The online version contains supplementary material available at https://doi.org/10.1038/s41567-022-01747-0.

Correspondence and requests for materials should be addressed to Ming Guo.

Peer review information *Nature Physics* thanks Alexandre Kabla and the other, anonymous, reviewer(s) for their contribution to the peer review of this work.

Reprints and permissions information is available at www.nature.com/reprints.

nature portfolio

Corresponding author(s): DBPR NPHYS-2021-07-01844B

Last updated by author(s): 2022/07/22

Reporting Summary

Nature Portfolio wishes to improve the reproducibility of the work that we publish. This form provides structure for consistency and transparency in reporting. For further information on Nature Portfolio policies, see our Editorial Policies and the Editorial Policy Checklist.

Statistics

For all statistical analyses, confirm that the following items are present in the figure legend, table legend, main text, or Methods section.

n/a	Confirmed	
☐	☒	The exact sample size (*n*) for each experimental group/condition, given as a discrete number and unit of measurement
☐	☒	A statement on whether measurements were taken from distinct samples or whether the same sample was measured repeatedly
☐	☒	The statistical test(s) used AND whether they are one- or two-sided *Only common tests should be described solely by name; describe more complex techniques in the Methods section.*
☒	☐	A description of all covariates tested
☒	☐	A description of any assumptions or corrections, such as tests of normality and adjustment for multiple comparisons
☐	☒	A full description of the statistical parameters including central tendency (e.g. means) or other basic estimates (e.g. regression coefficient) AND variation (e.g. standard deviation) or associated estimates of uncertainty (e.g. confidence intervals)
☐	☒	For null hypothesis testing, the test statistic (e.g. *F*, *t*, *r*) with confidence intervals, effect sizes, degrees of freedom and *P* value noted *Give P values as exact values whenever suitable.*
☒	☐	For Bayesian analysis, information on the choice of priors and Markov chain Monte Carlo settings
☒	☐	For hierarchical and complex designs, identification of the appropriate level for tests and full reporting of outcomes
☒	☐	Estimates of effect sizes (e.g. Cohen's *d*, Pearson's *r*), indicating how they were calculated

Our web collection on statistics for biologists contains articles on many of the points above.

Software and code

Policy information about availability of computer code

Data collection	LAS X is used to obtain the confocal microscopy images
Data analysis	Fiji (ImageJ) is used to track cell positions with time. Velocity correlation, multicellular flow analysis and Voronoi tessellation are all processes with customized codes in Matlab 2021a. OriginLab 2018 is used to analyze the data statistics in this study. All codes are available upon reasonable request.

For manuscripts utilizing custom algorithms or software that are central to the research but not yet described in published literature, software must be made available to editors and reviewers. We strongly encourage code deposition in a community repository (e.g. GitHub). See the Nature Portfolio guidelines for submitting code & software for further information.

Data

Policy information about availability of data

All manuscripts must include a data availability statement. This statement should provide the following information, where applicable:

- Accession codes, unique identifiers, or web links for publicly available datasets
- A description of any restrictions on data availability
- For clinical datasets or third party data, please ensure that the statement adheres to our policy

The datasets generated during and/or analysed during the current study are available from the corresponding author on reasonable request.

Field-specific reporting

Please select the one below that is the best fit for your research. If you are not sure, read the appropriate sections before making your selection.

☒ Life sciences ☐ Behavioural & social sciences ☐ Ecological, evolutionary & environmental sciences

For a reference copy of the document with all sections, see nature.com/documents/nr-reporting-summary-flat.pdf

Life sciences study design

All studies must disclose on these points even when the disclosure is negative.

Sample size	Five to ten samples are measured for each curvature in the fabricated wells experiment. 22 samples are measured for the alveolospheres.
Data exclusions	For fabricated wells, only wells with confluent cell layers are measured.
Replication	All the measurements were done at least in three independent experiments to verify the reproducibility of the experimental findings (precise number are given in the figure caption), and the results were consistent.
Randomization	Analyzed alveolospheres are chosen based on their size.
Blinding	The investigators were blinded to group allocation during data collection and analysis.

Reporting for specific materials, systems and methods

We require information from authors about some types of materials, experimental systems and methods used in many studies. Here, indicate whether each material, system or method listed is relevant to your study. If you are not sure if a list item applies to your research, read the appropriate section before selecting a response.

Materials & experimental systems

n/a	Involved in the study
☐	☒ Antibodies
☐	☒ Eukaryotic cell lines
☒	☐ Palaeontology and archaeology
☐	☒ Animals and other organisms
☒	☐ Human research participants
☒	☐ Clinical data
☒	☐ Dual use research of concern

Methods

n/a	Involved in the study
☒	☐ ChIP-seq
☒	☐ Flow cytometry
☒	☐ MRI-based neuroimaging

Antibodies

Antibodies used	Alexa Fluor 568 goat anti-rabbit IgG (H+L) (Thermo Fisher scientific, # A11036) E-Cadherin (24E10) Rabbit mAb (Cell Signaling, # 3195S) ZO-1 Monoclonal Antibody (ZO1-1A12) (Invitrogen, # 339100) ANTI-RABBIT IGG (H+L), CF568 (Sigma-Aldrich, # SAB4600084) ANTI-ZYXIN, DEVELOPED IN RABBIT, IGG FRA (Sigma-Aldrich, #Z4751) ANTI-VINCULIN ANTIBODY, MOUSE MONOCLONAL (Sigma-Aldrich, #V9264) ANTI-MOUSE-IGG - ATTO 647 (Sigma-Aldrich, #50185)
Validation	Alexa Fluor 568 goat anti-rabbit IgG (H+L) : https://www.thermofisher.com/antibody/product/Goat-anti-Rabbit-IgG-H-L-Highly-Cross-Adsorbed-Secondary-Antibody-Polyclonal/A-11036 E-Cadherin (24E10) Rabbit mAb: https://www.cellsignal.com//products/primary-antibodies/e-cadherin-24e10-rabbit-mab/3195?utm_strategy=lev&utm_conv=mon&utm_stage=ous&utm_tactic=ppc&utm_region=hq&gclid=CjwKCAjw0qOIBhBhEiwAyvVcf5lQI6j45x4QoS4dlp__EEpzT5LXp1NF6LxoA4AMJkUauOp1tTRkdhoC1kQQAvD_BwE&gclsrc=aw.ds ZO-1 Monoclonal Antibody (ZO1-1A12): https://www.thermofisher.com/antibody/product/ZO-1-Antibody-clone-ZO1-1A12-Monoclonal/33-9100 ANTI-RABBIT IGG (H+L), CF568: https://www.sigmaaldrich.com/US/en/product/sigma/sab4600084 ANTI-ZYXIN, DEVELOPED IN RABBIT, IGG FRA: https://www.sigmaaldrich.com/US/en/product/sigma/z4751 ANTI-VINCULIN ANTIBODY, MOUSE MONOCLONAL: https://www.sigmaaldrich.com/US/en/product/sigma/v9264 ANTI-MOUSE-IGG - ATTO 647: https://www.sigmaaldrich.com/US/en/product/sigma/50185

Eukaryotic cell lines

Policy information about cell lines

Cell line source(s)	The MDCK cell line was purchased from ATCC.
Authentication	The MDCK cell line was purchased from ATCC. And then the MDCK cells were transfected to stably express NLS-GFP.
Mycoplasma contamination	The MDCK cell line was tested negative for mycoplasma contamination by ATCC. We did not perform testing for the cell line.
Commonly misidentified lines (See ICLAC register)	No cell line listed by ICLAC was used.

Animals and other organisms

Policy information about studies involving animals; ARRIVE guidelines recommended for reporting animal research

Laboratory animals	The study did not involve laboratory animals.
Wild animals	The study did not involve wild animals.
Field-collected samples	The study did not involve samples collected from the field.
Ethics oversight	All experiments involving the differentiation of human iPSC lines were performed with the approval of the Institutional Review Board of Boston University (protocol H33122).

Note that full information on the approval of the study protocol must also be provided in the manuscript.